Title

Long-term electrode behavior during treatment of arsenic contaminated groundwater by a pilot-scale iron electrocoagulation system

Permalink

https://escholarship.org/uc/item/6cs0937d

Authors

Bandaru, Siva RS
Roy, Abhisek
Gadgil, Ashok J
et al.

Publication Date

2020-05-01

DOI

10.1016/j.watres.2020.115668

Peer reviewed

1   Long-term electrode behavior during treatment of arsenic contaminated

2   groundwater by a pilot-scale iron electrocoagulation system

3

4   Siva R. S. Bandaru[1], Abhisek Roy[2], Ashok J. Gadgil[1], Case M. van

5   Genuchten[3,4]*

6
7
8   [1]Department of Civil and Environmental Engineering, University of California, Berkeley,
9   Berkeley, California, USA
10
11   [2]Department of Civil Engineering, Jadavpur University, Kolkata, India
12
13   [3]Department of Earth Science - Geochemistry, Faculty of Geoscience, Utrecht University,
14   Utrecht, the Netherlands
15
16   [4]Department of Geochemistry, Geological Survey of Denmark and Greenland (GEUS),
17   Copenhagen, Denmark
18
19   *corresponding author:
20   cvg@geus.dk
21
22
23
24
25   **Keywords:** anodic dissolution, electrode surface layers, iron electrocoagulation, arsenic
26   removal, sustainable water treatment
27

28 **Abstract**

29   Iron electrocoagulation (Fe-EC) is an effective technology to remove arsenic (As) from

30 groundwater used for drinking. A commonly noted limitation of Fe-EC is fouling or passivation

31 of electrode surfaces via rust accumulation over long-term use. In this study, we examined the

32 effect of removing electrode surface layers on the performance of a large-scale (10000 L/d

33 capacity) Fe-EC plant in West Bengal, India. We also characterized the layers formed on the

34 electrodes in active use for over two years at this plant. The electrode surfaces developed three

35 distinct horizontal sections of layers that consisted of different minerals: calcite, Fe(III)

36 precipitates and magnetite near the top, magnetite in the middle, and Fe(III) precipitates and

37 magnetite near the bottom. The interior of all surface layers adjacent to the Fe(0) metal was

38 dominated by magnetite. We determined the impact of surface layer removal by mechanical

39 abrasion on Fe-EC performance by measuring solution composition (As, Fe, P, Si, Mn, Ca, pH,

40 DO) and electrochemical parameters (total cell voltage and electrode interface potentials) during

41 electrolysis. After electrode cleaning, the Fe concentration in the bulk solution increased

42 substantially from 15.2 to 41.5 mg/L. This higher Fe concentration led to increased removal of a

43 number of solutes. For As, the concentration reached below the 10 μg/L WHO MCL more

44 rapidly and with less total Fe consumed (i.e. less electrical energy) after cleaning (128.4 μg/L As

45 removed per kWh) compared to before cleaning (72.9 μg/L As removed per kWh). Similarly,

46 the removal of P and Si improved after cleaning by 0.3 mg/L/kWh and 1.1 mg/L/kWh,

47 respectively. Our results show that mechanically removing the surface layers that accumulate on

48 electrodes over extended periods of Fe-EC operation can restore Fe-EC system efficiency

49 (concentration of solute removed/kWh delivered). Since Fe release into the bulk solution

50 substantially increased upon electrode cleaning, our results also suggest that routine electrode

51 maintenance can ensure robust and reliable Fe-EC performance over year-long timescales.

1. Introduction

Nearly 200 million people worldwide are exposed to toxic concentrations of naturally occurring arsenic in groundwater used for drinking (Naujokas et al. 2013). Chronic arsenic exposure causes various types of internal cancers, cardiovascular and reproductive problems, and painful skin lesions that can result in gangrene and amputations (Smith et al. 2002; Smith et al. 1992; Steinmaus et al. 2013). The arsenic crisis is severe in South Asia due to the low income of the population, lack of resources and poor infrastructure of arsenic remediation technologies, especially in rural regions (Johnston et al. 2010; Amrose et al. 2015). Iron electrocoagulation (Fe-EC) is gaining attention as a promising technology to remove arsenic from groundwater in resource-poor settings. This technique is attractive because it has many properties that favor implementation and sustainable operation in rural communities, such as its modular design, low cost, flexible operation, low infrastructure requirements, and amenability to automation (Wan et al. 2011; Kumar et al. 2004; Amrose et al. 2014; Holt et al. 2005). In Fe-EC, a small external DC voltage is applied to Fe(0) plates to produce Fe(II) ions at the anode and $H_{2(g)}$ at the cathode (Lakshmanan et al. 2009; Chen 2004; Moreno et al. 2009). The Fe(II) ions generated at the anode migrate to the bulk solution, where dissolved oxygen (DO) can oxidize Fe(II) to form Fe(III) (oxyhydr)oxide precipitates, which have a strong arsenic sorption affinity (Hug and Leupin 2003). While Fe-EC has been well documented in laboratory studies to effectively remove arsenic to below the World Health Organization (WHO) maximum contaminant limit (MCL) of 10 µg/L (WHO 2018), rigorous field-based investigations of Fe-EC treatment remain poorly documented in the peer-reviewed literature, especially for large-scale plants operated over extended periods. Investigations of pilot-scale treatment systems are essential to characterize and address the technical challenges that arise when treatment methods emerge from the laboratory and begin extended operation in the field.

76   In the few field-based investigations of Fe-EC systems in the literature, it is commonly

77 reported that resistive rust surface layers form on the surfaces of Fe(0) electrodes over extended

78 operating cycles (Amrose et al. 2014, Hernandez et al. 2019, Timmes et al. 2010, van Genuchten

79 et al. 2016). These surface layers have been proposed to reduce the contaminant removal

80 efficiency (herein defined as the concentration of solute removed per electrical energy delivered;

81 $\mu g/L$ or mg/L per kWh) of Fe-EC systems. Although some studies have characterized the

82 surface layer mineralogy (Timmes et al. 2010; van Genuchten et al. 2016), the role of surface

83 layer growth on the performance of Fe-EC systems is not well understood. In theory, surface

84 layer growth can impact several aspects of EC treatment. First, electrochemically-generated

85 Fe(II) can be trapped in the electrode surface layer, which would decrease the amount of Fe(II)

86 transported to the bulk solution where it forms Fe(III) precipitates that bind solutes, such as

87 arsenic (As), phosphate (P) and silica (Si). Second, if the surface layer consists of poorly-

88 conducting Fe minerals (e.g. goethite, lepidocrocite), the rust build-up would increase the charge

89 transfer resistance, which increases the electrical energy required to pass current and could

90 increase the interface overpotential enough to favor anodic oxidation of H_2O to O_2 instead of

91 Fe(0) to Fe(II) (van Genuchten et al. 2017). Since the formation and growth of surface layers

92 can decrease the contaminant removal efficiency via these processes, surface layer removal is

93 likely an effective method to increase or maintain the performance of Fe-EC system.

94   Various techniques to mitigate surface layer growth have been proposed in the literature,

95 such as altering the frequency with which the electrode polarity is reversed, manipulating the

96 electrode storage conditions (air dried vs. wet storage) and periodic removal of the surface layers

97 by mechanical abrasion. Of these methods, mechanical removal of the surface layers seems to be

98 one of the most promising strategies. For example, in a recent extended laboratory study, Muller

99 et al. 2019 found that alternating the electrode polarity at both short and long frequencies

100 increased the surface layer mass relative to maintaining a single polarity and varying the

101   electrode storage conditions during inactive cycles was ineffective at preventing surface layer

102   growth. By contrast, periodic mechanical electrode cleaning (after days to weeks of operation)

103   effectively restored Fe-EC performance in the lab (Muller et al. 2019) and is an attractive field-

104   based approach because it is simple and requires only minimal, low-cost labor without hazardous

105   chemicals (Amrose et al. 2014; Nikolaev et al. 1982). However, few studies describe how the

106   performance of Fe-EC systems changes as a result of thorough electrode cleaning (i.e. with

107   mechanical abrasion to completely remove hard layers of rust build-up) and no studies have

108   investigated Fe-EC field systems with large electrodes (~18000 cm^2 per electrode) that have

109   operated over extended periods. Understanding how mechanical electrode cleaning impacts the

110   performance of fully-operational Fe-EC systems would help practitioners optimize plant

111   maintenance and operation and can be used to improve predictions of the long-term efficiency of

112   Fe-EC systems.

113   The objective of this work is to characterize the extent to which deep mechanical

114   cleaning of the electrodes restores the performance of a pilot-scale Fe-EC field system in a case

115   where the electrodes had not been cleaned after two years of use (in operation about 8 hours per

116   day, 2-4 days per week). For the purpose of this work, we use the term "deep cleaning" to

117   indicate thorough surface layer removal by mechanical abrasion with a hand-held angle grinder,

118   followed by thorough electrode washing with water. To this end, we performed a set of

119   experiments at an existing Fe-EC plant actively treating arsenic contaminated groundwater for

120   drinking at a rural school near Kolkata, India. To understand the effect of deep cleaning on Fe-

121   EC system performance, we compared an exhaustive series of chemical (As, Fe, P, Si, Mn, pH,

122   DO) and electrochemical parameters (total cell potential, electrode interface potentials) before

123   and after electrode deep cleaning. We also investigated the macroscopic (>1 mm) surface layer

124   properties using a high-resolution digital camera and determined the surface layer mineralogy

125   and composition using X-ray diffraction (XRD), X-ray absorption spectroscopy (XAS) and wet

126   chemical techniques. Our results reveal significant improvements in the contaminant removal

127   efficiency and operating costs of Fe-EC treatment following electrode deep cleaning. Our field-

128   based Fe-EC investigation provides important complementary perspectives to results derived

129   from laboratory-based Fe-EC studies, both of which are required for a complete understanding of

130   the potential of Fe-EC to sustainably improve safe water access in rural, arsenic-affected,

131   resource-poor communities.

132 **2. Materials and methods**

133 2.1 Description of the Fe-EC system and field site

134   The Fe-EC pilot plant is situated at Dhapdhapi High School, West Bengal, India and had

135 been in operation for two years prior to the experiments. To meet the local water demand, the

136 plant was operated for 2-4 days per week during the school year and two days per week when

137 school was out of session. The plant consisted of two steel reactor tanks coated with food grade

138 epoxy paint to house the electrode assembly (~1600 L for each tank; 1270 mm × 1210 mm ×

139 1030 mm). Both reactor tanks contained 16 parallel mild steel plates (IS 2062, cold formed, Shri

140 Hari Industries, Mumbai, India) spaced 50 mm apart, each with dimensions of 1000 mm × 900

141 mm × 3 mm. These mild steel plates (herein referred to as Fe(0) plates or electrodes for

142 simplicity) were used as received. Figure S1 in the Electronic Supplemental Material (ESM)

143 shows the unused electrodes as received. The 16 electrodes in each reactor tank were connected

144 electrically, such that alternating Fe(0) plates served as anode and cathode (8 anodes and 8

145 cathodes per tank, Fig. 1). The 16 electrodes in reactor tank 1 (RT1) are numbered as E1 to E16,

146 and those in reactor tank 2 (RT2) are numbered as E17 to E32. Both reactor tanks were open to

147 the atmosphere (Fig. 1). Before electrolysis, the tanks were filled with 1000 L of contaminated

148 groundwater from a nearby tube well (depth ~32 m) using a submersible pump at a flow rate of

149 22 L/min. The chemical composition of this groundwater is summarized in Table S1 in the

150 ESM, but notably contained 164±9 µg/L As.

151

152 2.2 Fe(0) electrolysis

153   We followed the exact Fe-EC electrolysis protocol as employed by the local Fe-EC plant

154 operators. After filling the reactor tanks, anodic Fe(0) dissolution was initiated by applying a

155 direct current of 150 A (current density, i, = 0.3 mA/cm^2) for approximately 90 min to the 32

156 electrodes housed in both tanks with a custom-built power supply (Suresh Electrical Industries,

157   India) under ambient atmospheric conditions. A total coulombic dose of 450 C/L (2.3 mM Fe by

158   Faraday's law) was applied in experiments before and after electrode deep cleaning (described

159   below). Following existing practices, we varied the total cell voltage manually to maintain

160   constant current throughout electrolysis. The polarity of all electrodes was reversed after each

161   experiment. During electrolysis, the solution was mixed by recirculating 5.25 reactor volumes

162   per hour using a centrifugal pump. These operating parameters were used in experiments before

163   and after electrode deep cleaning.

164

165   <u>2.3 Mechanical removal of the electrode surface layers</u>

166   Electrode deep cleaning was performed by first removing all Fe(0) plates from the reactor

167   tanks and letting the electrodes air dry overnight on a clean floor cover. When dried, the mass of

168   each electrode plate was measured using a hanging scale (procured locally). Next, selected

169   surface layer sections were sampled for subsequent characterization by gently removing the

170   layers with a brass scraper in the top, middle, and bottom regions of representative Fe(0) plates.

171   Since the solids accumulated on the electrode surface contained several layers, a series of

172   scrapings from the outer and inner layers at a single location was also collected. In addition to

173   surface layer samples, the As-laden Fe(III) precipitate sludge produced during routine Fe-EC

174   treatment was collected from the Fe-EC plant tube settler. The surface layers and raw sludge

175   were stored in clean-sealed plastic bags prior to analysis by X-ray diffraction (XRD), X-ray

176   absorption spectroscopy (XAS) and acid digestions.

177   After collecting surface layer samples from >10 different electrodes across both reactor

178   tanks, the remaining surface layers were removed from each electrode using angle grinders fit

179   with a metallic wire brush for removing rust from steel. To maintain the structural integrity of

180   the electrodes during deep cleaning, minimal pressure was applied while using the angle

181   grinders. After electrode deep cleaning, each Fe(0) plate was rinsed with water to remove

182   residual surface flakes and the electrodes were left to dry overnight. The mass of each electrode

183   was then measured again using a hanging scale to quantify mass loss from deep cleaning. A

184   high-resolution digital camera was used to photograph the electrodes before and after deep

185   cleaning. The electrodes were then re-inserted into their respective positions in the reactor tanks

186   and were reconnected to the power supply.

187

188   <u>2.4 Solid phase analysis</u>

189   Major and minor mineral phases in the surface layers were identified by powder XRD

190   and XAS. For XRD, the surface layer samples were ground into a fine powder with a mortar and

191   pestle. A Bruker D-8 diffractometer was used to collect the diffractograms (Cu K-α radiation)

192   from 15-75° 2θ (0.01° step sizes) using a rotating sample stage. X-ray absorption spectra at the

193   Fe K-edge were collected for a subset of samples at beam line 4-1 of the Stanford Synchrotron

194   Radiation Lightsource and at the Dutch-Belgian beam line (DUBBLE, BM-26a) of the European

195   Synchrotron Facility (Nikitenko et al. 2008; Borsboom et al. 1998). Additional details of XAS

196   data collection and analysis are provided in the SI.

197   The chemical composition of the solids was determined by digesting surface layer

198   samples and the raw treatment sludge using an aqua regia solution (70% HNO_3 and 37% HCl,

199   1:3 mol ratio) following published protocols (van Genuchten et al. 2016). The digestion was

200   then analyzed for Fe, As, P, Si, Ca, and Mn by inductively-coupled plasma optical emission

201   spectrometry (ICP-OES, Perkin Elmer Optima 8000).

202

203   <u>2.5 Bulk solution and electrochemical measurements</u>

204   A series of water samples was collected at regular time intervals during Fe(0) electrolysis

205   before and after deep cleaning to evaluate the effect of surface layer removal on solution

206   chemistry. While the reactors were filling with groundwater, aliquots of raw, unfiltered water

207   were collected in 15 mL sample vials for measurements of the initial electrolyte composition.

208   After the current was applied, unfiltered aliquots of the bulk solution were collected using a wide

209   mouth pipette every 10 min during electrolysis for measurements of total Fe generated by Fe-EC.

210   In addition, filtered samples were collected at identical 10 min intervals by passing a suspension

211   aliquot through 0.2 µm nylon filters for measurements of dissolved ions. A few drops of

212   concentrated nitric acid (70%) were added to 5 ml of each filtered and unfiltered sample and the

213   final volume was adjusted to 10 mL by adding DI water. All samples were sealed to the

214   atmosphere and transported to the home institution for analysis of Fe, As, P, Si, Ca, and Mn by

215   ICP-OES.

216   Bulk solution pH and DO were measured initially and throughout electrolysis using a

217   Thermo Scientific Orion pH meter and Hach LDO optical DO probe, respectively. The initial

218   pH and DO were measured in RT1 at a depth of ~25 cm before initiating electrolysis. During

219   electrolysis, pH and DO measurements were collected at 10 min intervals at the same location in

220   RT1.

221   The interfacial potentials (IP) of the electrodes (anodes and cathodes) were measured

222   after the current stabilized (10 min after onset of electrolysis) using an Ag/AgCl reference

223   electrode and a handheld multimeter (Fluke). The IP of each electrode was measured by

224   submerging the Ag/AgCl reference electrode to a depth of 12-13 cm and placing the tip of the

225   reference electrode adjacent to the Fe(0) plate. Current flowing through each Fe(0) plate was

226   measured with a handheld AC/DC clamp meter (Fluke 376 True RMS). All measurements

227   except pH and DO are plotted as an average of values from RT1 and RT2. Identical protocols

228   for bulk solution and electrochemical measurements were followed in experiments before and

229   after electrode deep cleaning.

230

231   **3. Results**

232   3.1 Macroscopic characteristics of the electrodes

233   Fig. 2 shows the macroscopic surface characteristics of a representative Fe(0) plate

234   before (Fig. 2A) and after (Fig. 2B) electrode deep cleaning. The surface of the Fe(0) plate

235   before cleaning (Fig. 2A) had three visually distinct regions, labeled A-I, A-II and A-III based on

236   color and surface texture. The top (A-I) approximately 1/3 of the plate was characterized by

237   light orange surface layers with smooth uniform texture. The middle (A-II) region, which was

238   also approximately 1/3 of the electrode, showed black surface layers with a heterogeneous

239   texture consisting of large (2-5 cm diameter) oblate, dome-shaped blisters. The bottom (A-III)

240   1/3 of the electrode was a closer match to the A-I region, but had thicker and dark orange surface

241   layers covered with smaller (<1 cm diameter) blisters. These three distinct regions were

242   observed for both sides of every electrode, except for those at the ends of each electrode

243   assembly (end-plates E1 and E16 in RT1 and E17 and E32 in RT2). The sides of the four end-

244   plates that faced the bulk electrolyte displayed surface layers of uniform light orange color

245   without blisters (Fig. S2). The sides of these end-plates that faced the electrode assembly

246   resembled the remaining electrodes with A-I, A-II and A-III regions.

247   Electrode deep cleaning (described in Section 2.3) removed significant quantities of the

248   surface layers that had accumulated on the electrodes over two years. On average, 2.3±0.4 kg

249   (Table S2) of surface layers was removed from each electrode, which was >10% of the initial

250   average electrode mass (21.7±0.6 kg). Removing the surface layers resulted in smooth black

251   surfaces for all regions (B-I, B-II and B-III, Fig. 2B). Visual inspection of the electrodes after

252   deep cleaning revealed a near complete transformation of the middle region (B-II) to a black

253   heterogeneous texture, rather than the smooth shiny surface indicative of Fe(0) metal in the B-I

254   and B-III regions. Electrode deep cleaning around large blisters (2-5 cm diameter) resulted in

255   significant material loss in the form of large flakes (1-2 cm diameter, 0.2-0.5 mm thickness),

256   which produced depressions in the electrodes. Additional cleaning around blisters in the middle

257   of the electrode might have resulted in cleaner surfaces (Fig. 2B), but more rigorous cleaning

258   was not attempted in this region to avoid structural damage to the electrode.

259

260   3.2 Surface layer characterization

261   *3.2.1 Mineralogy.* In Fig. 3, we present XRD patterns of surface layer samples from the

262   three characteristic locations (A-I, A-II and A-III) showing different colors and textures for a

263   representative electrode (E31). In addition, Fig. 3 presents the XRD patterns of samples

264   collected at different depths of the surface layer at a single location (E22 exterior, interior). The

265   XRD patterns showed differences in the intensity of characteristic diffraction peaks depending

266   on the sample location and depth. For example, the Bragg diffraction peak of calcite ($CaCO_3$) is

267   more intense in the sample collected from the A-I region of the electrode, which also had the

268   lightest color. Bragg diffraction peaks from goethite (α-FeOOH) and lepidocrocite (γ-FeOOH)

269   were also more apparent in the A-I and A-III surface layers than in the A-II region. Peaks from

270   calcite and lepidocrocite were absent in the XRD pattern of the sample collected from the black

271   middle region (A-II); only peaks due to magnetite (Fe_3O_4) appeared in this diffractogram. The

272   extended X-ray absorption fine structure (EXAFS) spectra of the samples collected from the A-I,

273   A-II and A-III regions showed trends consistent with the XRD patterns, but suggest a larger

274   contribution of disordered Fe(III) precipitates. The EXAFS spectra of the A-I and A-III surface

275   layers display characteristic fingerprints of nanocrystalline 2-line ferrihydrite (Fig. S4), which

276   was not apparent in the diffractograms. The EXAFS spectrum of the A-II surface layer matched

277   more closely that of magnetite. Comparing the diffractograms of samples collected from the

278   interior and exterior of a single location (Fig. 3) showed that the light-colored exterior contained

279   more Fe(III) precipitates and calcite, whereas magnetite dominated the interior adjacent to the

280   Fe(0) metal.

281   Figure 4 shows the powder XRD patterns of homogenized flakes (~1-3 cm diameter) of

282   surface layers collected from 10 different electrodes. All surface layer samples exhibited

283   diffractograms with similar features, but slightly varied peak amplitudes. The diffractograms

284   indicate that magnetite is a major component of the surface layers, regardless of the plate

285   position in the electrode assembly, but we note that disordered Fe(III) precipitates could be

286   present and not display strong peaks in the XRD patterns. In addition to the widespread presence

287   of magnetite, nearly all surface layer samples showed Bragg peaks from goethite, and to a lesser

288   extent, lepidocrocite, which is consistent with previous studies of the surface layers formed on

289   Fe-EC electrodes over shorter timescales (Timmes et al. 2010; van Genuchten et al. 2016).

290   Bragg diffraction peaks for calcite were observed in many samples, but were more intense in the

291   light-colored samples, consistent with the XRD patterns of A-I surface layers of E31 (Fig. 3).

292   *3.2.2 Chemical composition.* In Table 1, we present the chemical composition of

293   identical surface layer samples as those for which XRD patterns are given in Fig. 3. For

294   comparison, Table 1 also lists the chemical composition of the air-dried Fe(III) precipitate bulk

295   sludge collected from the tube settler after one Fe-EC run. Along the height of the plate, the

296   mass fraction of Fe (532 g/kg) was highest in the A-II region, consistent with the predominance

297   of magnetite, which has a higher theoretical Fe mass fraction (724 g/kg for Fe_3O_4) than goethite

298   (629 g/kg for FeOOH) and ferrihydrite (523 g/kg for $Fe(OH)_3$). In contrast, the mass fractions of

299   As (55 mg/kg), Si (3.1 g/kg) and Ca (1.9 g/kg) were lowest in the A-II region. In general, the A-

300   I and A-III regions contained the highest fraction of oxyanions (As = 72-158 mg/kg; Si = 5.4-5.5

301   g/kg; P = 497-654 mg/kg) and Ca (24.6-42.9 g/kg), which is consistent with the higher fraction

302   of poorly-ordered, reactive Fe(III) precipitates and calcite in these regions. However, Mn had a

303   relatively uniform distribution in the three regions (770-1060 mg/kg). Within a single surface

304   layer, the mass fractions of all elements except Fe were 2-5 times higher at the exterior than the

305   interior (Table 1).

306   All surface layer samples displayed higher mass fractions of Fe (435-532 g/kg) than the

307   air-dried bulk treatment sludge generated during Fe-EC (186 g/kg Fe). The bulk treatment

308   sludge also contained 3-30 times higher oxyanion mass fractions (Table 1) than any of the

309   surface layers. By contrast, the Ca and Mn mass fractions of the treatment sludge (Ca = 71.3

310   g/kg; Mn = 885 mg/kg) were relatively similar to the electrode surface layers. The overall trends

311   in surface layer composition tabulated for electrode 31 (E31) in Table 1 were comparable for all

312   measured surface layers collected from other electrodes (Table S2).

313

314   <u>3.3 Behavior of the chemical composition of the bulk electrolyte</u>

315   *3.3.1 Iron production*. In Fig. 5, we report the average concentration of total Fe (aqueous

316   plus solid phase) measured in the bulk electrolyte throughout electrolysis before and after

317   electrode deep cleaning. The gray bar in Fig. 5 represents the expected bulk Fe concentration

318   based on Faraday's law, assuming all charge passed through the anode goes to the production

319   and release of Fe(II) to the bulk solution (i.e. 100% Faradaic efficiency). Before electrode deep

320   cleaning, the bulk Fe concentration remained near its initial value of 13.7±2.2 mg/L throughout

321   the delivery of 450 C/L, indicating poor production of Fe in bulk solution. By contrast, the bulk

322   Fe concentration after electrode deep cleaning increased roughly linearly with electrolysis time,

323   leading to 41.5 mg/L at the end of electrolysis. Although the Fe level increased substantially

324   after electrode deep cleaning, the 41.5 mg/L measured after cleaning is still below the expected

325   concentration (117.0 mg/L) assuming 100% Faradaic efficiency, which could be due to

326   inadequate mixing during electrolysis and settling of Fe(III) solids. We also note that laboratory

327   experiments using brand new electrodes of the same material as those of the Fe-EC pilot plant in

328   the current investigation measured a Faradaic efficiency in synthetic groundwater of

329   approximately 80% (Muller et al. 2019).

330   *3.3.2 Dissolved arsenic, phosphate, silicate and manganese.* Fig. 6 compares the residual

331   fractions of dissolved As, P, Si and Mn in the bulk solution before and after deep cleaning of

332   electrode. Electrode cleaning resulted in more rapid removal of As, P, Si and Mn. For example,

333   the As concentration decreased from the initial 164±9 µg/L to <10 µg/L within 60 min of

334   electrolysis after electrode deep cleaning, whereas ~90 minutes of electrolysis was required to

335   reach 10 µg/L using uncleaned electrodes. Similar to As removal, the removal of P was

336   improved after electrode deep cleaning. Fig. 6B shows that after 20 min of Fe(0) electrolysis,

337   98% of the initial 1.6±0.3 mg/L P was removed after deep cleaning compared to just 74% at the

338   same stage of electrolysis using uncleaned electrodes. Electrode deep cleaning also resulted in

339   an increase in Si removal (initial Si = 15.3±1.7 mg/L) from nearly no removal with the uncleaned

340   electrodes to 28% removal at the end of electrolysis (Fig. 6C). Consistent with the removal of

341   oxyanions, the removal fraction of initial Mn (5.8±0.3 mg/L) increased from 12% before

342   electrode deep cleaning to 21% (Fig. 6D). Taken together, electrode deep cleaning improved the

343   removal of all measured species per kWh (Table S3).

344

345   3.4 Electrochemical parameters.

346   The behavior of the cell potential as a function of electrolysis time (Fig. 7) was similar

347   for experiments before and after deep cleaning, with a rapid increase in voltage immediately

348   after the onset of electrolysis, followed by a gradual increase. However, the curve of the total

349   cell potential was positioned ~2 V lower for the experiment following electrode deep cleaning

350   (6.2 to 9.9 V) relative to that before cleaning (7.8 to 11.8 V). This lower voltage required to pass

351   the 150 A current resulted in lower energy consumed over the course of electrolysis from 2.2

352   kWh before cleaning to 1.6 kWh after cleaning. Consistent with the reduction in total cell

353   potential after deep cleaning, the average anodic interface potential became less positive,

354   decreasing from 3.0±0.9 to 2.1±0.6 V vs Ag/AgCl for all anodes in RT1 and RT2 (Fig. S5). The

355 average cathodic interface potential also became less negative after deep cleaning (-2.2±0.5 to -

356 1.5±0.5 V vs Ag/AgCl for all cathodes electrodes in RT1 and RT2). Measurements of the

357 current for individual plates (Table S4) indicated the 150 A applied to both RT1 and RT2 was

358 well distributed among all plates (9.7 A per plate) except for those facing the bulk electrolyte

359 (E1, E16, E17, E32), which had less current (7.1 per plate).

360

361 <u>3.5 Dissolved oxygen and pH.</u>

362   Fig. 8 shows the behavior of the DO and solution pH in the bulk electrolyte throughout

363 electrolysis before and after electrode deep cleaning. Consistent with the reducing conditions of

364 the aquifer that provided the raw water, low initial DO concentrations were measured before

365 Fe(0) electrolysis. Before deep cleaning, the DO concentration reached air-saturation (>9 mg/L)

366 after 80 min of electrolysis, where it stayed for the remainder of the experiment. After deep

367 cleaning, the DO level increased more slowly and stabilized near 7 mg/L, several mg/L below

368 the air-saturated value.

369   The behavior of solution pH throughout electrolysis (Fig. 8B) followed similar trends for

370 experiments before and after electrode deep cleaning. In both sets of experiments, the solution

371 pH steadily increased during electrolysis, consistent with cathodic H^+ reduction to $H_{2(g)}$, after a

372 short 15 min lag where it stayed near its initial value of 7.1. Although the shape of the pH curve

373 as a function of electrolysis time was similar for experiments before and after deep cleaning, the

374 increase in pH with electrolysis time was smaller after electrode deep cleaning (final pH near

375 7.5) than before deep cleaning (final pH near 7.7).

376   **4. Discussion**

377   4.1. Physical characteristics of surface layers formed during extended Fe-EC field treatment

378   *4.1.1 Formation of three distinct electrode surface regions.* The XRD and XAS data of surface

379   layer samples suggest widespread magnetite formation adjacent to the Fe(0) metal (i.e. the

380   interior surface layer) extending over the entire electrode surface, with layers of calcite and

381   Fe(III) precipitates adhered to the surface layer exterior of the A-I and A-III regions. The

382   formation and growth of magnetite on Fe-EC electrodes has been documented by a number of

383   field and laboratory Fe-EC studies (Müller et al. 2019; van Genuchten et al. 2016; Timmes et al.

384   2010). The predominance of magnetite in our work is attributed to the initial product of Fe-EC

385   treatment being Fe(II) and the high thermodynamic stability of magnetite across a wide range of

386   solution composition (i.e. pH, redox conditions) when Fe(II) is present (Cornell and

387   Schwertmann 2003). The existence of magnetite in the surface layer interior is a concern

388   because it has been proposed to trap electrochemically-generated Fe(II), which increases

389   magnetite layer growth at the expense of Fe(II) transport to the bulk solution where As removal

390   occurs. Magnetite formation is also important because its conductivity, though lower than bare

391   Fe(0) metal, is orders of magnitude higher than that of most Fe(III) precipitates (e.g.

392   lepidocrocite, goethite) and calcite, which is beneficial for the flow of current.

393   The greater abundance of calcite and Fe(III) precipitates in the exterior surface layers of

394   the A-I and A-III regions is attributed to the design of the Fe-EC reactor. Though speculative,

395   one explanation for preferential calcite formation near the electrode top is the proximity of this

396   region to the air-water interface. This proximity could facilitate calcite formation by more

397   effective $CO_{2(g)}$ exchange with the atmosphere (exsolving increases pH and favors calcite

398   formation) or by mixing-induced splashes near the water surface enhancing evaporation and

399   leading to locally increased Ca^{2+} and CO_3^{2-} activity. The color and abundance of Fe(III)

400   precipitates in the A-III region of all 32 electrodes is likely related to the accumulation of settled

401   solids at the bottom of the reactor tanks. Due to the flat bottom of the reactor tanks and

402   insufficient pumping of the post-electrolysis suspension to the tube settler, a constant layer of

403   settled particles remained in the tanks after water transfer. This layer of accumulated sludge

404   consisted of the poorly-ordered Fe(III) precipitates formed during typical Fe-EC treatment (Fig.

405   S4) and was ~10 cm deep under stagnant conditions. However, when the tanks were filled and

406   mixed, a fraction of this layer became resuspended, leading to a dense region of solids near the

407   bottom of the reactor, consistent with the adherence of orange, poorly-ordered Fe(III)

408   precipitates to the A-III region of the electrode (Fig. 2, Fig. S4). While the light-colored surface

409   layers in the A-I and A-III regions can inhibit Fe(II) transport to the bulk solution similar to

410   magnetite, these surface layers also likely lead to inhomogeneous electron flow through the

411   electrodes. The insulating surface layer minerals (e.g. calcite, Fe(III) precipitates) in the A-I and

412   A-III regions are expected to result in preferential electron flow through the A-II region. This

413   conclusion is consistent with the significant quantities of uncorroded Fe(0) metal in the A-I and

414   A-III regions observed after deep cleaning (Fig. 2B) and only a few spots of bare Fe(0) metal in

415   the A-II region, suggesting nearly complete electrochemical oxidation of the center of the

416   electrode.

417   *4.1.2 Blisters.* In addition to the three horizontal regions of distinct surface layers,

418   another major modification of the electrode surface was the formation of protruding blisters (2-5

419   cm wide) of rusted Fe(0) metal. These blisters were most abundant and had the largest diameter

420   in the A-II region (Fig. 2B), where the electrodes were likely most electrochemically active, but

421   blistering was observed to a lesser extent in the A-I and A-III regions. These unique features can

422   be explained by the cathodic reduction of H^+. The reaction occurring at the cathode most

423   commonly reported in the Fe-EC literature is the reduction of $2H^+$ to form $H_{2(g)}$ that bubbles to

424   the water surface. However, it is well documented that H^+ reduction can also yield adsorbed H

425   atoms that diffuse into the Fe(0) crystal lattice to occupy microstructural defect sites, such as

426 vacancies, dislocations and grain boundaries (Landolt 2007; Jiang and Carter 2004; Bockris et al.

427 1965). At these sites, $H_{2(g)}$ build-up from H atom recombination can create local areas of high

428 internal pressure, which causes deformation and pushes the material towards the surface,

429 consistent with our observations of dome-shaped blisters (Laureys et al. 2017; Escobar et al.

430 2011). Since the electrode polarity of the investigated Fe-EC system was reversed between

431 every test (i.e. each electrode served as cathode and anode), every electrode was blistered. The

432 only regions without blisters were the sides of the four end-plates (E1, E16, E17, E32) facing the

433 bulk electrolyte (Fig. S2), which is consistent with their lower current and interface potentials

434 (Table S4, Fig. S5).

435   The formation of relatively large blisters is a concern for Fe-EC system operation

436 because they worsen the structural integrity of the Fe(0) electrodes. Because Fe-EC is based on

437 forming Fe(II) by the oxidation of the Fe(0) anode (often termed the *sacrificial* anode), it is

438 inevitable that the electrodes must be replaced when all Fe(0) metal has been oxidized.

439 However, the electrode must be replaced more quickly if uncorroded Fe(0) is still present, but

440 the electrode fails structurally. In our work, deep cleaning of a blister on one electrode removed

441 a large flake of magnetite, leaving a small hole in the plate. Removal of many similarly large

442 flakes could therefore result in large holes and failure of the electrode structure, which would

443 lead to the premature loss of beneficial, uncorroded Fe(0) metal. However, we note that so long

444 as the structural integrity of the electrode is maintained, the formation of large blisters is

445 expected to be less consequential to Fe-EC performance than the coating of the electrode surface

446 by insulating layers of calcite and Fe(III) precipitates.

447

448 4.2 Influence of electrode deep cleaning on solution chemistry

449   *4.2.1 Iron.*   The optimization of Fe-EC performance relies on efficient electrochemical

450 Fe(II) production and transport to the bulk solution. We found that electrode deep cleaning

451 increased the bulk Fe concentration after electrolysis from <15 mg/L to 41.5 mg/L, a nearly 3-

452 fold improvement, and decreased the total cell voltage by ~2V. We note that bulk Fe levels

453 might have continued to increase following the electrolysis stage due to insufficient electrolyte

454 mixing, but no measurements were collected after the current stopped. This clear improvement

455 in Fe release to solution after electrode deep cleaning provides compelling field-based evidence

456 to confirm the hypothesis that electrode surface layers block the transport of electrochemically

457 generated Fe(II) to the bulk electrolyte. Because the production and release of Fe(II) from the

458 electrode initiates the removal of many chemical species in Fe-EC, the increased bulk Fe level

459 coincided with more effective removal of As, P, Si and Mn and modified the behavior of DO and

460 solution pH. The chemical dynamics of As, DO and pH before and after cleaning are discussed

461 below, with P, Si and Mn removal described in section S2 of the ESM.

462 *4.2.2 Arsenic*. Before deep cleaning, ~90 min of Fe(0) electrolysis was required to

463 remove 164±9 µg/L As to below the 10 µg/L WHO MCL, which equated to >2.2 kWh (average

464 voltage of 9.9 V). It is noteworthy that the uncleaned electrodes still achieved adequate As

465 removal despite poor bulk Fe production, which could be partly due to the high raw water Fe

466 content and the resuspension of reactive Fe(III) precipitates that had settled in the reactor tank

467 bottoms during previous runs. After deep cleaning, only 60 min of electrolysis was required to

468 achieve <10 µg/L As, which equated to 1.3 kWh (average voltage of 8.4 V). Therefore, if

469 electrolysis ceased after 60 min when the As level decreased to <10 µg/L, the As removal

470 efficiency would be nearly twice as high after electrode deep cleaning (increase from 72.9 to

471 128.4 µg/L As per kWh). However, additional electrolysis time included as a factor of safety

472 resulted in only 20% higher As removal efficiency after electrode deep cleaning (increase from

473 72.9 to 86.4 µg/L/kWh). Previous laboratory studies of Fe-EC systems operated at similar

474 charge dosage rates as the pilot plant indicate that arsenic removal typically proceeds through a

475 two-step pathway (Li et al. 2012, van Genuchten et al. 2012, van Genuchten et al. 2020): i)

476   oxidation of arsenite (As(III)), the dominant species in reduced aquifers (Roberts et al. 2004), by

477   reactive Fenton-type oxidants (e.g. Fe(IV)) generated by Fe(II) reactions with DO and ii)

478   arsenate (As(V)) sorption to co-precipitating Fe(III) (oxyhydr)oxides. This reaction pathway is

479   supported by As K-edge XAS measurements of the arsenic-rich sludge collected directly from

480   the pilot plant, which indicated that As(V) is the overwhelmingly dominant form of arsenic

481   bound to the solids (Roy et al. 2019). Since both reaction steps are initiated by Fe(II), the

482   improvement in As removal efficiency can be explained by the increased bulk Fe concentration

483   and the lower total cell voltage (hence lower electrical energy consumption) after electrode deep

484   cleaning. We note briefly here that while the sludge contains strongly-sorbing As(V), appropriate

485   sludge disposal is still necessary because aqueous As can leach even from As(V)-rich Fe(III)

486   oxides when the solids are exposed to reducing conditions (e.g. organic-rich soils). In the short

487   term, the sludge generated at the plant is being used by researchers at Jadavpur University for

488   investigating its immobilization in concrete blocks (Roy et al. 2019). For the long term, a

489   contract has been signed with a state-approved hazardous waste disposal company (Ramky Ltd.)

490   for removing sludge for storage at a hazardous chemical waste disposal site at Haldia, West

491   Bengal (Hernandez et al. 2019).

492   Another outcome of removing and characterizing the electrode surface layers is the

493   ability to perform a mass balance calculation of As on a large Fe-EC system to confirm the As

494   removal location. Averaging the composition of surface layer samples measured in this work

495   (Table S2) gives a surface layer As content of 51.7±39.5 mg/kg. Multiplying this value by the

496   surface layer mass removed during deep cleaning gives a total of 3.82±2.92 g of As attached to

497   the electrode. During the two years of surface layer growth, the plant treated ~900 m^3 of

498   groundwater from 164±9 to <10 µg/L As (i.e. at least 154 µg/L removed), yielding 138.6 g of

499   total As removed. These calculations indicate that As attachment to the electrode surface

500   accounted for <3% of total removal, which supports the conclusion that As is removed

21

501   dominantly by sorption to Fe(III) precipitates in the bulk (Kumar et al. 2004). We note that the

502   As content of the light-colored layers was several times higher than for magnetite, suggesting

503   that the As fraction bound to the electrodes would decrease further if Fe(III) precipitate build-up

504   on the electrode was avoided.

505   *4.2.2 Dissolved oxygen and solution pH*. In addition to altering the dynamics of ion

506   removal, electrode deep cleaning also affected the behavior of DO and solution pH.

507   Measurements of DO during experiments with both unclean and clean electrodes revealed a

508   continuous increase from the low initial value (<2.0 mg/L) throughout electrolysis, which

509   indicates that the flux of atmospheric O_2 into the electrolyte was greater than O_2 consumption

510   during Fe-EC treatment. However, the final DO was ~2 mg/L lower after deep cleaning than

511   before, which can be explained by the more efficient production of Fe(II) with clean electrodes,

512   which consumes DO to form Fe(III) precipitates (Delaire et al. 2017). In experiments with both

513   unclean and clean electrodes, the solution pH increased steadily during electrolysis, which is

514   explained by a combination of both $CO_{2(g)}$ outgassing and the consumption of H^+ ions at the

515   cathode. However, after deep cleaning, the pH increase was 0.15-0.2 log units lower than before

516   deep cleaning. This result is attributed to the higher bulk Fe concentration after deep cleaning

517   because Fe(II) oxidation and Fe(III) hydrolysis consumes OH^-, thus lowering pH.

518

519   4.3 Recommendations for maintaining and operating Fe-EC systems

520   Proper maintenance of water treatment technologies is critical to ensure their sustained

521   operation in optimal conditions. This is particularly important when operating in rural, resource-

522   poor areas where small changes in overall treatment costs and power consumption can render

523   technologies ineffective or economically unviable. In our study, we investigated one of the only

524   documented Fe-EC pilot plants that has sustainably removed arsenic from local groundwater in

525   South Asia for extended periods (about 4 years at the time of this writing). Studying this unique

526   system, we found that mechanically removing the magnetite, calcite and Fe(III) precipitate

527   surface layers formed on Fe(0) electrodes over extended operation improved dramatically the

528   performance of the system. For example, surface layer removal resulted in a substantial increase

529   in bulk Fe production and a decrease in the voltage (and hence in the electrical energy

530   consumption) required to pass the 150 A of current needed for treatment. These improvements

531   led to a significant increase in arsenic removal efficiency (128.4 µg/L As removed per kWh after

532   cleaning, 72.9 µg/L As removed per kWh before cleaning). These results imply that periodic,

533   on-schedule electrode cleaning to completely remove accumulated surface layers can help to

534   sustain the performance of Fe-EC systems over year-long timescales. Based on cost estimates of

535   local labor and electricity use, our cost-benefit analysis (Table S5) suggests that the cleaning

536   procedure was economically practical, but we note that the success criteria for maintaining

537   different Fe-EC plants will depend on regional costs of labor and electricity and several

538   properties of the plant (e.g. size, influent arsenic concentration, price of steel, etc).

539   Among the various approaches to maintain Fe-EC electrodes reported in the literature

540   (e.g. ultrasonic cleaning, high electrolyte velocity gradients: see section S3 in the ESM),

541   mechanical abrasion is one of the most attractive for rural communities in South Asia because

542   this method is simple, reliable and low-cost (Amrose et al. 2014, Hernandez et al. 2019, Timmes

543   et al. 2010, van Genuchten et al. 2016). Although this method requires some labor and

544   equipment, only three minimally trained workers were able to perform the deep cleaning in less

545   than two days, indicating the relative ease of the task. This suggests that the entire procedure

546   could be completed in a single weekend, which would prevent disrupting water treatment and

547   distribution to students, teachers, and staff during hours when the school that houses the pilot

548   plant is open. While polarity reversal has been proposed as a method to minimize surface layer

549   growth, our results suggest that this strategy had minimal effect, which is consistent with a

550   laboratory Fe-EC study showing polarity reversal actually increased surface layer growth over

551   extended operation (Muller et al. 2019). One promising alternative could be to operate the

552   system at high current densities (i.e. $i >$3 mA/cm^2), which was recently shown at the lab-scale to

553   limit surface layer formation (Muller et al. 2019), but this approach has not been tested on large

554   Fe-EC systems and can result in unacceptably high voltages. Hence, we propose that mechanical

555   deep cleaning is one of the most promising methods to improve bulk Fe(II) production and

556   decrease energy requirements, which is essential to achieve consistent As removal over sustained

557   periods.

558   The precise timing of electrode cleaning will depend on the operating conditions and

559   reactor design of the specific Fe-EC system, but our study has uncovered some useful

560   relationships to help optimize and simplify the cleaning schedule. One of the most obvious

561   indicators of Fe-EC performance and a useful trigger for electrode maintenance is the bulk Fe

562   concentration, which could be monitored regularly using field test kits (Merrill et al. 2009)

563   However, routine Fe measurements require trained labor and can be prohibitively expensive,

564   particularly in poor, decentralized communities. Instead, a number of other indicators could be

565   used, including the DO, solution pH and total cell potential. In our work, we found that

566   behaviors of the DO, pH and the cell voltage were all impacted by deep cleaning, with

567   systematic changes concomitant with an increase in bulk Fe concentration. These parameters are

568   simple to measure using hand-held devices, with unambiguous numerical values (as opposed to

569   color-based test kits). Therefore, plant operators without formal education can easily track the

570   behavior of the DO, pH and cell voltage and compare the values produced using clean electrodes

571   with those of old electrodes to make more informed decisions of when to begin an electrode deep

572   cleaning activity.

573   Finally, with respect to electrode blistering, we found that intensive mechanical cleaning

574   around blisters could lead to holes through the electrode, which should be avoided to maintain

575   the structural integrity of the electrode. Therefore, we recommend that electrode deep cleaning

576   preferentially targets the light-colored external electrode surface layers, which are significantly

577   more insulating than the magnetite interior layers and are the region most likely to overlay bare

578   Fe(0) metal. In addition, different types of steel of can be used as the electrode material since the

579   steel production process can impact the likelihood of blister formation. For example, a recent

580   study showed that cold formed steel allows the growth of blisters more than recovered and

581   recrystallized steel because of a greater number of structural defects (Laureys et al. 2017). The

582   electrode material used in the investigated Fe-EC system was cold formed steel, which could

583   contribute to the large sized blisters. Since H^+ reduction is likely related to blister formation,

584   selecting electrode materials that favor other cathodic reactions, such as carbon-based air-

585   diffusion cathodes that reduce O_2 form OH^- or H_2O_2 (Jiang et al. 2018) could also prevent the

586   electrode blistering observed in this work.

587

588   **5. Conclusions**

589   •   Thick surface layers formed on Fe-EC electrodes following operation over two years,

590   which inhibited Fe(II) transport to the bulk electrolyte. Surface layer growth occurred

591   despite polarity reversal between tests.

592   •   Three distinct horizontal surface layer regions formed: Fe(III) precipitates, calcite and

593   magnetite at the top, magnetite in the middle and Fe(III) precipitates and magnetite at the

594   bottom. The surface layer stratification is attributed to the operating conditions and Fe-

595   EC reactor design.

596   •   The middle region of all electrodes, which was dominated by magnetite and likely the

597   most electrochemically active area, consisted of 2-5 cm blisters attributed to cathodic H^+

598   reduction and H diffusion into the Fe(0) metal.

599   •   Mechanical removal of the surface layers increased substantially the bulk Fe

600   concentration, decreased total cell voltage and improved the removal efficiency of As and

601   other ions.

602   •   Our work suggests that periodic, on-schedule electrode cleaning by mechanical abrasion

603   can sustain Fe-EC performance over year-long timescales.

604

605 **6. Acknowledgements**
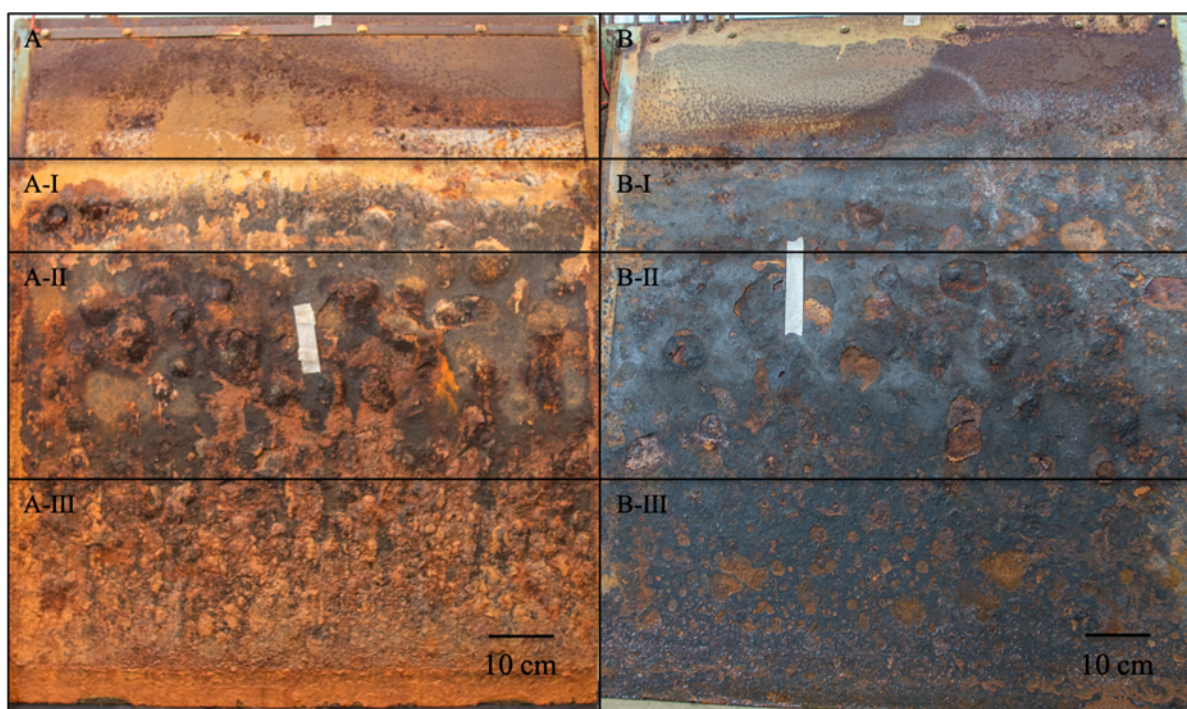
617

618   **Figure Captions**
619
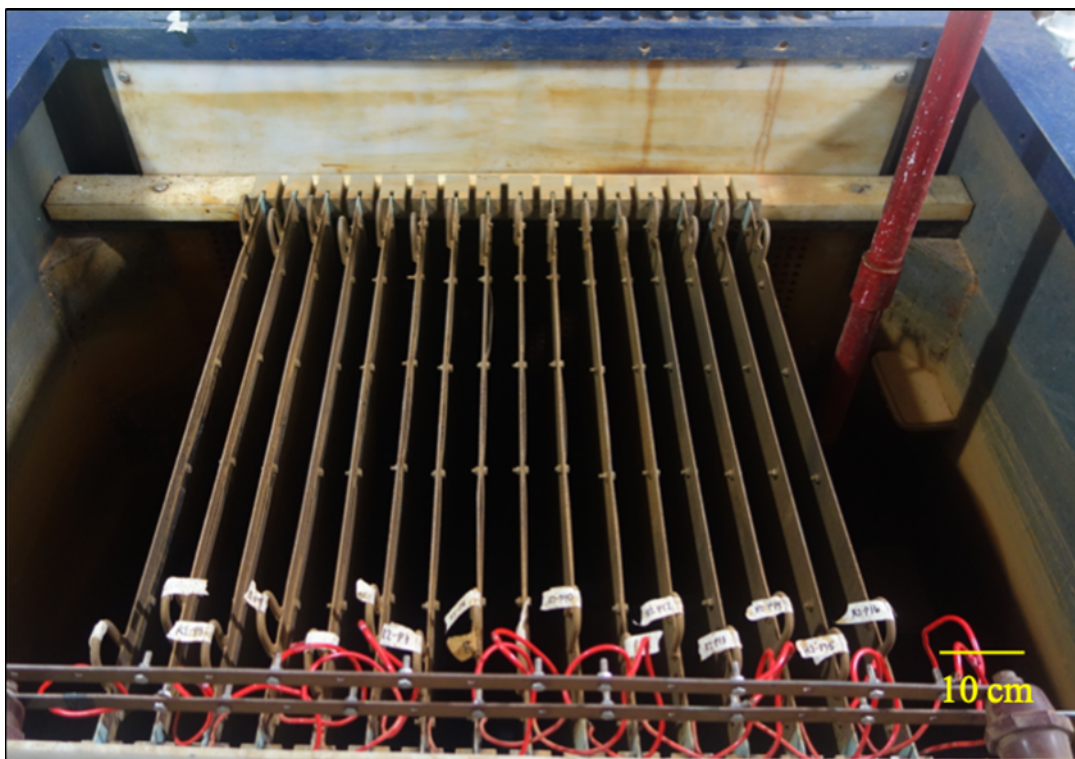
620
621
622   Fig. 1: Top view of the electrode assembly in reactor tank 1. Electrodes shown in this picture are
623   numbered E1 to E16 (left to right). This electrode layout was reproduced in reactor tank 2,
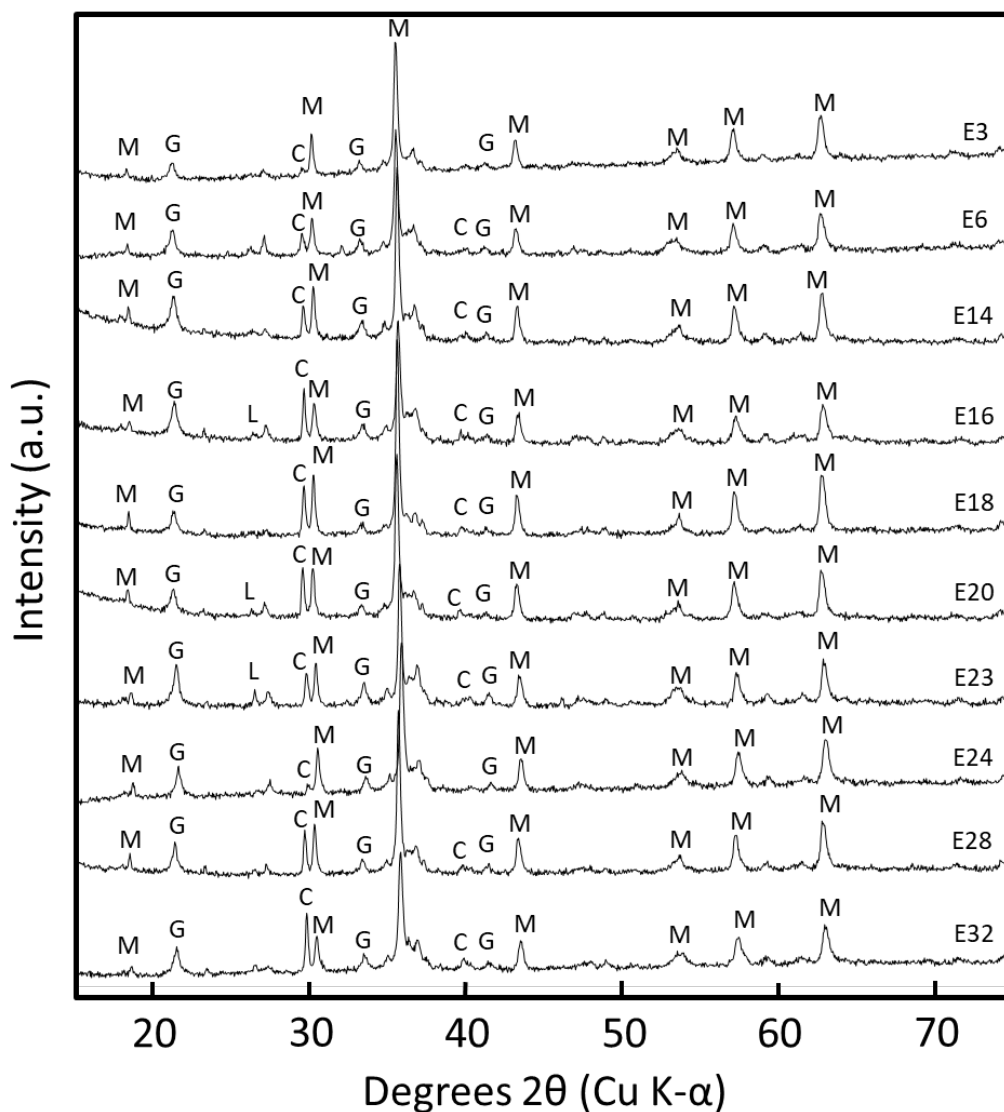624   which housed electrodes E17 to E32.
625
626

Fig. 2: A) Digital images representative electrodes before (A) and after (B) deep cleaning. All electrodes before deep cleaning displayed the A-I (top), A-II (middle) and A-III (bottom) regions. The regions above A-I and B-I were not in contact with the electrolyte solution during electrolysis and showed relatively little rust accumulation. The tape stuck to the electrode surface was added to help scale the dome-shaped blisters.
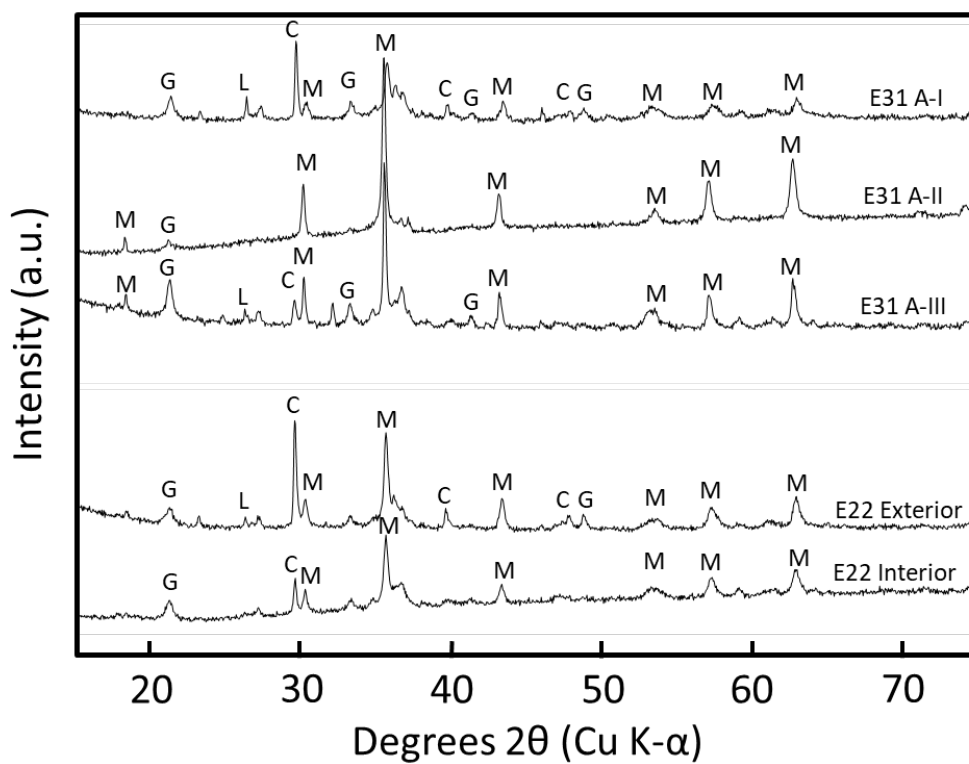
636
637
638   Fig. 3: Powder XRD patterns of surface layers collected from different regions of electrode E31
639   (A-I, A-II, A-III) and electrode E22 (Exterior, Interior). The letters M, G, L and C represent the
640   diffraction peaks of magnetite, goethite, lepidocrocite and calcite, respectively.
641
642

Fig. 4: Powder XRD patterns of surface layers collected from select electrodes. The letters M, G, L and C represent the diffraction peaks of magnetite, goethite, lepidocrocite and calcite, respectively.
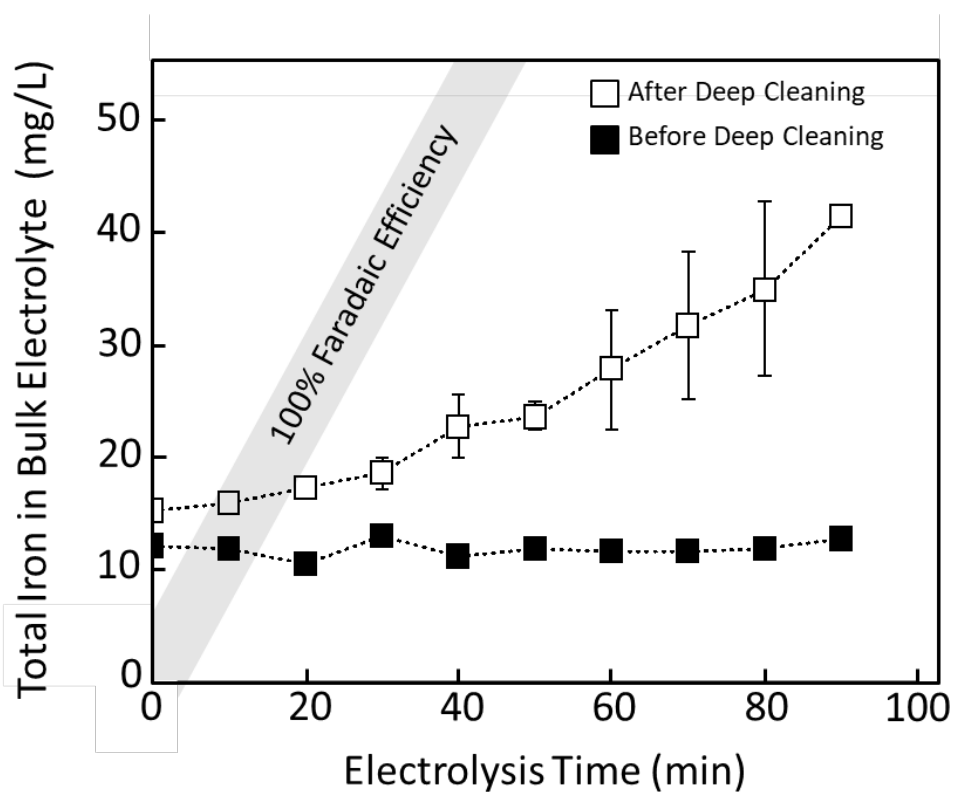
650
651
652 Fig. 5: Total (aqueous plus solid phase) iron concentration in the bulk electrolyte as a function
653 of electrolysis time, for experiments before (black squares) and after electrode deep cleaning
654 (white squares). 450 C/L was delivered by Fe(0) electrolysis over approximately 90 minutes.
655 The gray shaded region indicates the value expected based on 100% Faradaic efficiency.
656
657
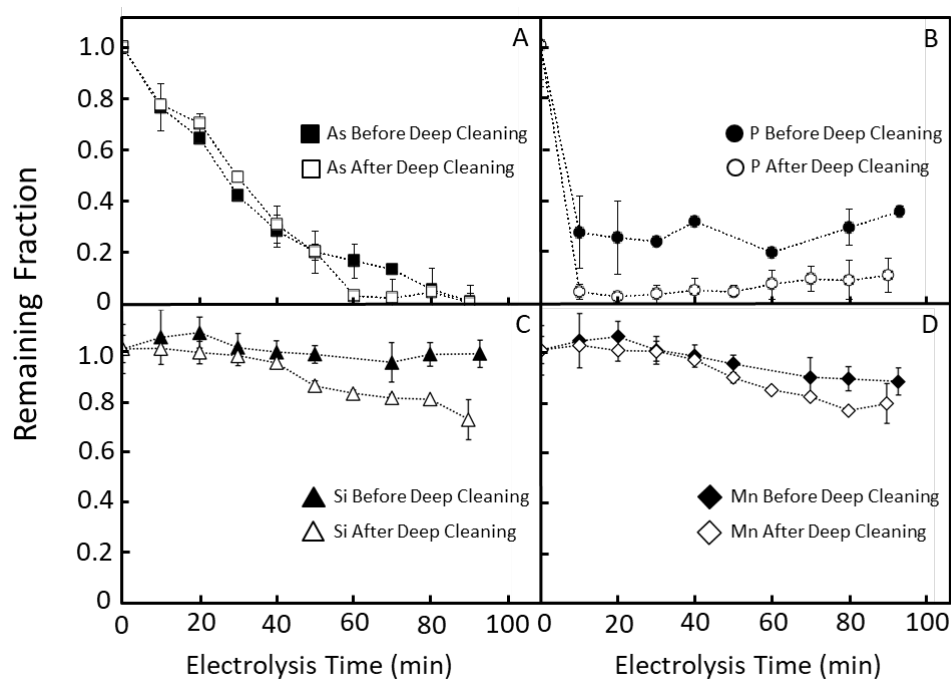
658
659
660   Fig. 6: Fraction of initial aqueous arsenic (A), phosphate (B), silicate (C) and manganese (D)
661   remaining in the bulk solution as a function of electrolysis time. The black diamonds indicate
662   measurements before deep cleaning, whereas the white diamonds indicate measurements after
663   deep cleaning.
664
665

33
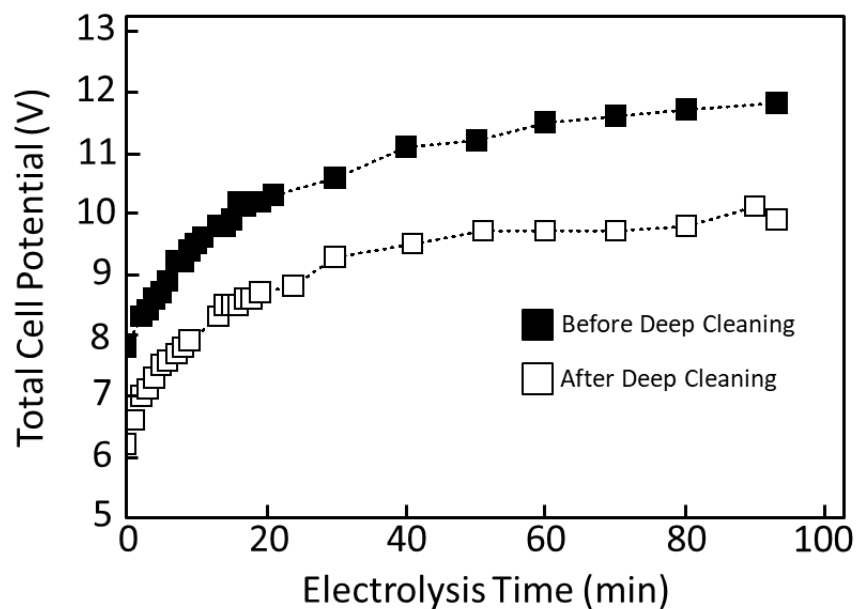
666
667
668   Fig. 7: Total cell potential as a function of electrolysis time for experiments before (black
669   squares) and after (white squares) electrode deep cleaning.
670
671
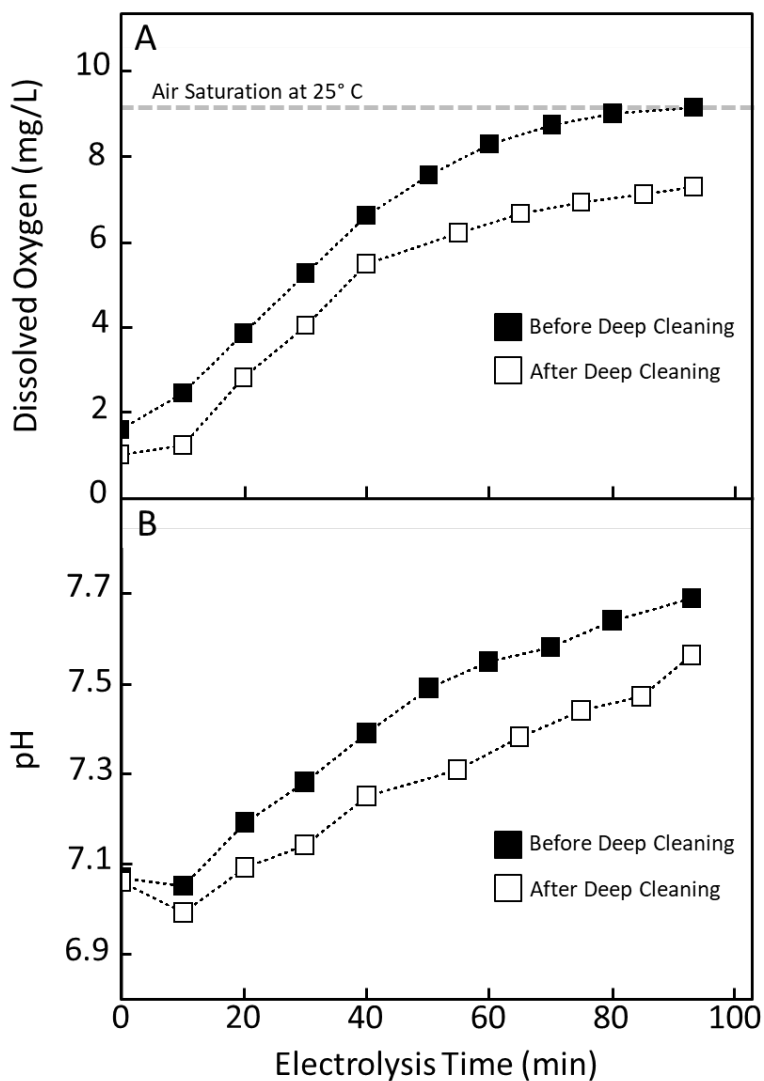
Fig. 8: Dissolved oxygen (top panel) and solution pH (bottom panel) as a function of electrolysis time for experiments before (black squares) and after (white squares) electrode deep cleaning. Data points represent measurements in reactor tank 1.

679   **Table 1: Chemical composition of air-dried sludge and select electrode surface layers**

Sample Name	Chemical Composition										
	Fe (g/kg)	As (mg/kg)	As/Fe (mol%)	P (mg/kg)	P/Fe (mol%)	Si (mg/kg)	Si/Fe (mol%)	Ca (g/kg)	Ca/Fe (mol%)	Mn (mg/kg)	Mn/Fe (mol%)
Air Dried Sludge	186	864.0	0.346	5320	5.16	6684	7.16	71.3	53.5	885	0.48
E31Region A-I	450	158.2	0.026	497	0.20	5507	2.43	42.9	13.3	1057	0.24
E31Region A-II	532	55.0	0.008	658	0.22	3072	1.15	1.9	0.50	1006	0.19
E31 Region A-III	435	71.9	0.012	654	0.27	5388	2.46	24.6	7.89	770	0.18
E22 Exterior	456	245.0	0.040	761	0.30	5268	2.30	69.9	21.4	1174	0.26
E22 Interior	460	ND	ND	348	0.14	1281	0.55	15.8	4.78	880	0.19

680   Values were obtained from aqua regia digestions. The remaining mass fraction is attributed to oxygen.
681

References

Amrose, S., Z. Burt, and I. Ray. 2015. Safe Drinking Water for Low-Income Regions, *Annual Review of Environment and Resources, Vol 40*, 40: 203-31.

Amrose, S. E., S. R. S. Bandaru, C. Delaire, C. M. van Genuchten, A. Dutta, A. DebSarkar, C. Orr, J. Roy, A. Das, and A. J. Gadgil. 2014. Electro-chemical arsenic remediation: Field trials in West Bengal, *Science of the Total Environment*, 488: 543-50.

Amrose, S., A. Gadgil, V. Srinivasan, K. Kowolik, M. Muller, J. Huang, and R. Kostecki. 2013. Arsenic removal from groundwater using iron electrocoagulation: Effect of charge dosage rate, *Journal of Environmental Science and Health Part a-Toxic/Hazardous Substances & Environmental Engineering*, 48: 1019-30.

Borsboom, M, W Bras, I Cerjak, D Detollenaere, DG van Loon, P Goedtkindt, M Konijnenburg, P Lassing, YK Levine, B Munneke, M Oversluizen, R van Tol, and E Vlieg. 1998. The Dutch-Belgian beamline at the ESRF, *Journal of Synchrotron Radiation*, 5: 518-20.

Chen, G. H. 2004. Electrochemical technologies in wastewater treatment, *Separation and Purification Technology*, 38: 11-41.

Cornell, R. M. and Schwertmann, U. 2003. *The iron oxides: structure, properties, reactions, occurrences and uses*. John Wiley & Sons. Marcus, P. ed., 2011. Corrosion mechanisms in theory and practice. CRC press.

Delaire, C., S. Amrose, M. H. Zhang, J. Hake, and A. Gadgil. 2017. How do operating conditions affect As(III) removal by iron electrocoagulation ?, *Water Research*, 112: 185-94.

Escobar, D. P., C. Minambres, L. Duprez, K. Verbeken, and M. Verhaege. 2011. Internal and surface damage of multiphase steels and pure iron after electrochemical hydrogen charging, *Corrosion Science*, 53: 3166-76.

Hernandez, D., K. Boden, P. Paul, S.R.S. Bandaru, S. Mypati, A. Roy, S.E. Amrose, J. Roy, A.J. Gadgil. 2019. Strategies for successful field deployment in a resource-poor region: Arsenic remediation technology for drinking water, *Development Engineering*, 4.

Holt, P. K., G. W. Barton, and C. A. Mitchell. 2005. The future for electrocoagulation as a localised water treatment technology, *Chemosphere*, 59: 355-67.

Hug, S. J., and O. Leupin. 2003. Iron-catalyzed oxidation of arsenic(III) by oxygen and by hydrogen peroxide: pH-dependent formation of oxidants in the Fenton reaction, *Environmental Science & Technology*, 37: 2734-42.

Jiang, D.E. and Carter, E.A. 2004. Diffusion of interstitial hydrogen into and through bcc Fe from first principles. *Physical Review B*, *70*(6), p.064102.

Jiang, Y. Y., P. J. Ni, C. X. Chen, Y. Z. Lu, P. Yang, B. Kong, A. Fisher, and X. Wang. 2018. Selective Electrochemical H2O2 Production through Two-Electron Oxygen Electrochemistry, *Advanced Energy Materials*, 8.

Johnston, R. B., S. Hanchett, and M. H. Khan. 2010. The socio-economics of arsenic removal, *Nature Geoscience*, 3: 2-3.

Kumar, P. R., S. Chaudhari, K. C. Khilar, and S. P. Mahajan. 2004. Removal of arsenic from water by electrocoagulation', *Chemosphere*, 55: 1245-52.

Lakshmanan, D., D. A. Clifford, and G. Samanta. 2009. Ferrous and Ferric Ion Generation During Iron Electrocoagulation, *Environmental Science & Technology*, 43: 3853-59.

Landolt, Dieter. 2007. *Corrosion and surface chemistry of metals* (EPFL Press ; CRC Press distributor: Lausanne Boca Raton, FL).

Laureys, A., E. Van den Eeckhout, R. Petrov, and K. Verbeken. 2017. Effect of deformation and charging conditions on crack and blister formation during electrochemical hydrogen charging, *Acta Materialia*, 127: 192-202.

731 Merrill, R. D., A. A. Shamim, A. B. Labrique, H. Ali, K. Schulze, M. Rashid, P. Christian, and
732   K. P. West. 2009. Validation of two Portable Instruments to Measure Iron concentration
733   in Groundwater in rural Bangladesh, *Journal of Health Population and Nutrition*, 27:
734   414-18.
735 Moreno, H. A., D. L. Cocke, J. A. G. Gomes, P. Morkovsky, J. R. Parga, E. Peterson, and C.
736   Garcia. 2009. Electrochemical Reactions for Electrocoagulation Using Iron Electrodes,
737   *Industrial & Engineering Chemistry Research*, 48: 2275-82.
738 Müller, S., T. Behrends, and C. M. van Genuchten. 2019. Sustaining efficient production of
739   aqueous iron during repeated operation of Fe(0) electrocoagulation, Water Research, 155:
740   455-464.
741 Naujokas, M. F., B. Anderson, H. Ahsan, H. V. Aposhian, J. H. Graziano, C. Thompson, and W.
742   A. Suk. 2013. The Broad Scope of Health Effects from Chronic Arsenic Exposure:
743   Update on a Worldwide Public Health Problem, *Environmental Health Perspectives*, 121:
744   295-302.
745 Nikitenko, S, AM Beale, AMJ van der Eerden, SDM Jacques, O Leynaud, MG O'Brien, D
746   Detollenaere, R Kaptein, BM Weckhuysen, and W Bras. 2008. Implementation of a
747   combined SAXS/WAXS/QEXAFS set-up for time-resolved in situ experiments, *Journal*
748   *of Synchrotron Radiation*, 15: 632-40.
749 Nikolaev, NV, AS Kozlovskii, and II Utkin. 1982. Treating natural waters in small water
750   systems by filtration with electrocoagulation, *Soviet Journal of Water Chemistry and*
751   *Technology*, 4: 244-47.
752 Roberts, L. C., S. J. Hug, T. Ruettimann, M. Billah, A. W. Khan, and M. T. Rahman. 2004.
753   Arsenic removal with iron(II) and iron(III) in waters with high silicate and phosphate
754   concentrations, *Environmental Science & Technology*, 38: 307-15.
755 Roy, A., van Genuchten, C.M., Mookherjee, I., Debsarkar, A. and Dutta, A. 2019. Concrete
756   stabilization of arsenic-bearing iron sludge generated from an electrochemical arsenic
757   remediation plant. *Journal of environmental management*, *233*, pp.141-150.
758 Smith, A. H., C. Hopenhayn-Rich, M. N. Bates, H. M. Goeden, I. Hertz-Picciotto, H. M.
759   Duggan, R. Wood, M. J. Kosnett, and M. T. Smith. 1992. Cancer risks from arsenic in
760   drinking water, *Environ Health Perspect*, 97: 259-67.
761 Smith, A. H., P. A. Lopipero, M. N. Bates, and C. M. Steinmaus. 2002. Public health - Arsenic
762   epidemiology and drinking water standards, *Science*, 296: 2145-46.
763 Steinmaus, C. M., C. Ferreccio, J. A. Romo, Y. Yuan, S. Cortes, G. Marshall, L. E. Moore, J. R.
764   Balmes, J. Liaw, T. Golden, and A. H. Smith. 2013. Drinking water arsenic in northern
765   chile: high cancer risks 40 years after exposure cessation, *Cancer Epidemiol Biomarkers*
766   *Prev*, 22: 623-30.
767 Tiegel, M. C., M. L. Martin, A. K. Lehmberg, M. Deutges, C. Borchers, and R. Kirchheim. 2016.
768   Crack and blister initiation and growth in purified iron due to hydrogen loading, *Acta*
769   *Materialia*, 115: 24-34.
770 Timmes, T. C., H. C. Kim, and B. A. Dempsey. 2010. Electrocoagulation pretreatment of
771   seawater prior to ultrafiltration: Pilot-scale applications for military water purification
772   systems, *Desalination*, 250: 6-13.
773 van Genuchten, C.M., Addy, S.E., Peña, J. and Gadgil, A.J. 2012. Removing arsenic from
774   synthetic groundwater with iron electrocoagulation: an Fe and As K-edge EXAFS study.
775   *Environmental science & technology, 46*(2), pp.986-994.
776 van Genuchten, C. M., S. R. S. Bandaru, E. Surorova, S. E. Amrose, A. J. Gadgil, and J. Pena.
777   2016. Formation of macroscopic surface layers on Fe(0) electrocoagulation electrodes
778   during an extended field trial of arsenic treatment, *Chemosphere*, 153: 270-79.

779 van Genuchten, C. M., K. N. Dalby, M. Ceccato, S. L. S. Stipp, and K. Dideriksen. 2017. Factors
780   affecting the Faradaic efficiency of Fe(0) electrocoagulation, *Journal of Environmental*
781   *Chemical Engineering*, 5: 4958-68.
782 van Genuchten, C. M., and J. Pena. 2017. Mn(II) Oxidation in Fenton and Fenton Type Systems:
783   Identification of Reaction Efficiency and Reaction Products, *Environmental Science &*
784   *Technology*, 51: 2982-91.
785 van Genuchten, C. M., T. Behrends, S. L. S. Stipp, and K. Dideriksen. 2020. Achieving arsenic
786   concentrations of <1 ug/L, by Fe(0) electrolysis: The exceptional performance of
787   magnetite. *Water Research*, 168: 115170.
788 Wan, W., T. J. Pepping, T. Banerji, S. Chaudhari, and D. E. Giammar. 2011. Effects of water
789   chemistry on arsenic removal from drinking water by electrocoagulation, *Water*
790   *Research*, 45: 384-92.
791 WHO. 2018. Developing drinking-water quality regulations and standards: general guidance
792   with a special focus on countries with limited resources. In. Geneva: World Health
793   Organization. Licence: CC BY-NC-SA 3.0 IGO.